A&A, 711, A188 (2026)
https://doi.org/10.1051/0004-6361/202660529


Astronomy & Astrophysics

# Tidal tails and mass segregation in nearby open clusters with *Gaia* DR3

Wenchang Zhao[1,2], Jing Chen[1,⋆], Yujun Tang[1], Xuran He[1], Zhengke Deng[1], Lishuai Huang[1], Lin Fu[1], Huanbin Chi[3], and Su Zhang[1,⋆]

[1] Dali University, No. 2, Hongsheng Road, Gucheng, Dali, Yunnan 671003, China
[2] Institute of Astrophysics, Central China Normal University, Wuhan 430079, China
[3] School of Artificial Intelligence, Yunnan Open University, Kunming 650599, China

Received 21 April 2026 / Accepted 10 June 2026

**ABSTRACT**

*Context.* Tidal tails trace open-cluster (OC) disruption, while mass segregation reflects internal relaxation. Yet faint OC tails are difficult to detect against dense Galactic backgrounds, and their connection to internal mass stratification remains poorly tested.
*Aims.* Using *Gaia* DR3, we analyze 65 nearby OCs ($d < 500$ pc, age >50 Myr) in a homogeneous search for tidal tails and for the role of mass segregation in their formation.
*Methods.* We used Forest Fire Clustering (FFC) for membership, combined 3D principal component analysis (PCA) with $L_z$–$E$ verification to identify tails, derived fundamental parameters with PARSEC v2.0 isochrones, quantified mass segregation with the minimum spanning tree (MST), and assessed relaxation through dynamical timescales.
*Results.* We detect tidal tails in nine OCs, including five new cases (HSC 2765, Mamajek 2, Platais 12, Theia 711, UBC 11), spanning 40–170 pc and tending to align toward the Galactic center. All nine show significant mass segregation ($\Lambda_{\rm MSR} > 1$): massive stars are centrally concentrated, whereas low-mass stars populate the outskirts. This supports a coupled evolutionary picture in which two-body relaxation moves low-mass stars outward and the Galactic tidal field strips them to form tails. Internal relaxation plus external stripping therefore appears to dominate the evolution of nearby evolved OCs.

**Key words.** Galaxy: disk – galaxies: star clusters: general

## 1. Introduction

Tidal tails are extended debris formed as star clusters lose members through internal dynamics and the Galactic tidal field (Baumgardt & Makino 2003; Just et al. 2009; Küpper et al. 2010). They are common in globular clusters but remain difficult to detect in open clusters (OCs). Although long predicted (Küpper et al. 2010), unambiguous OC tails became detectable only with high-precision *Gaia* astrometry, first in the Hyades (Röser et al. 2019; Meingast & Alves 2019; Jerabkova et al. 2021) and later in several dozen nearby systems identified by systematic searches (Tarricq et al. 2022; Bhattacharya et al. 2022; Kos 2024; Risbud et al. 2025). Most OCs lie near the Galactic plane, where dense backgrounds and low masses create weak phase-space overdensities, making tails hard to isolate (Jadhav et al. 2025). Detecting them is therefore essential for constraining cluster disruption and Galactic tidal heating.

*Gaia* DR3 has transformed studies of OC disruption, moving the field from isolated discoveries to systematic mapping and dynamical characterization (Tarricq et al. 2022; Kos 2024; Risbud et al. 2025). Probabilistic methods can now trace tails to kiloparsec scales (Kroupa et al. 2024), with Kos (2024) identifying candidate tails in 476 OCs. Model-independent convergent-point methods also reveal nearby tails and their kinematic substructure (Risbud et al. 2025). Attention has also shifted from morphology alone to internal tail properties, including binary content and kinematic asymmetry, which provide stronger constraints on disruption models (Pang et al. 2023), as shown for five OCs by Sharma et al. (2025).

Mass segregation, the concentration of massive stars toward cluster centers through two-body relaxation (Spitzer & Shull 1975), is closely linked to this process. As energy equipartition proceeds, low-mass stars drift outward and become easier for the Galactic tidal field to strip (Baumgardt & Makino 2003). Mass segregation thus provides the internal pathway that feeds tidal-tail formation. Although it has been reported in individual OCs (Tarricq et al. 2022; Childs et al. 2024; Zwicker et al. 2024; Motherway et al. 2024; Angelo et al. 2025; Zhang 2026), its prevalence in a well-defined sample of clusters with confirmed tails has not been tested systematically. While Sharma et al. (2025) analyzed the tail morphology, binary content, and rotation in five OCs, their sample was preselected from clusters with known tails and did not quantify mass segregation. Our study differs in three respects: it applies a homogeneous blind search to a larger distance- and age-limited sample of 65 OCs, combines three-dimensional morphology with independent $L_z$–$E$ confirmation to reduce projection-induced false positives, and explicitly links detected tails to internal mass segregation.

Despite this progress, low-contrast and irregular tails remain difficult to detect because of projection, contamination, and incomplete phase-space information. Here we present a homogeneous *Gaia* DR3 census of 65 nearby OCs. We re-derived membership with the Forest Fire Clustering (FFC) algorithm (Chen et al. 2022; Wei et al. 2025; Zhang et al. 2025), then identified and validated tails with complementary morphological and

⋆ Corresponding authors: chenjing05@tsinghua.org.cn; zhangsu77@dali.edu.cn

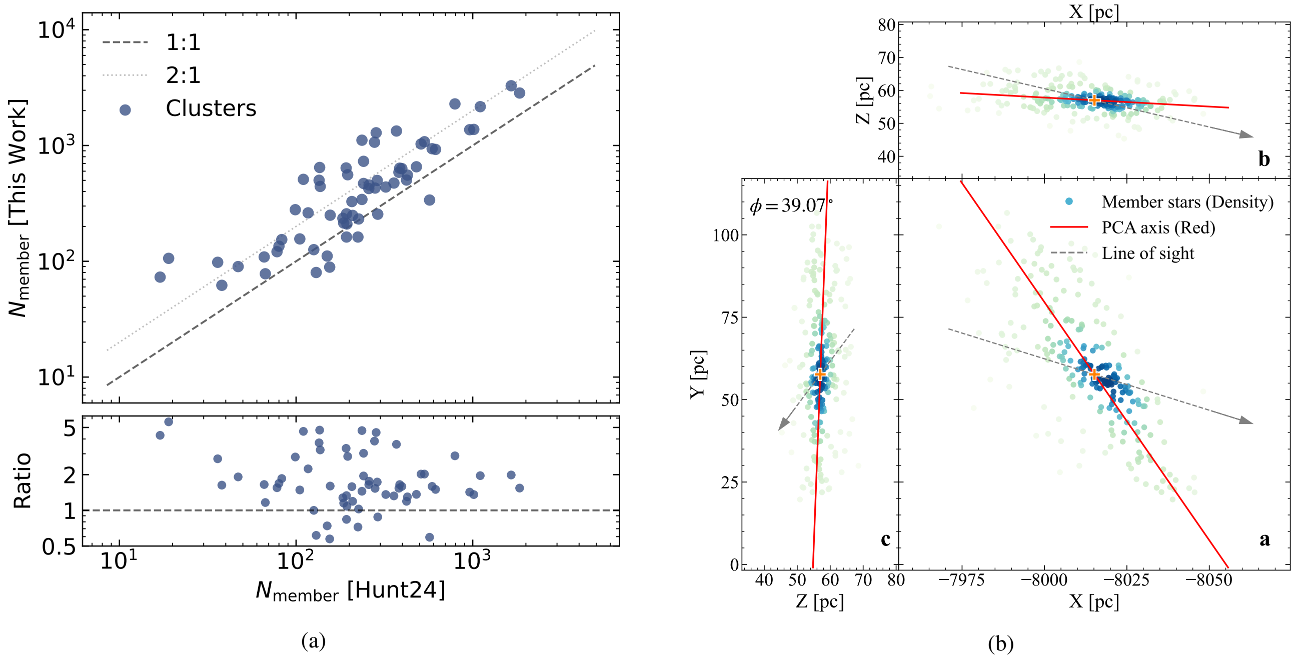


**Fig. 1.** Member recovery and morphological analysis. Panel a: comparison of cluster member counts (Prob > 0.5) between this work ($N_{\rm ThisWork}$) and HR23 ($N_{\rm HR23}$). The top subpanel shows the direct comparison, where the dashed line represents a 1:1 relation. The bottom subpanel displays the ratio $N_{\rm ThisWork}/N_{\rm HR23}$ as a function of $N_{\rm HR23}$. Most clusters lie above the 1:1 line, highlighting the systematic improvement in member recovery. Panel b: morphology of the high-$\phi$ cluster Mamajek 2 in Galactocentric Cartesian coordinates. The red line indicates the direction of the first principal axis from the 3D PCA, and the dashed gray line represents the line of sight from the Sun to the cluster center (orange cross).

dynamical diagnostics. We find tails in nine clusters, including five new cases. These structures extend 40–170 pc, tend to align toward the Galactic center, and contain stellar populations consistent with their parent clusters. All nine systems show mass segregation, directly supporting a coupled internal–external evolutionary pathway. By reducing false positives and method dependence, this work provides a unified benchmark for OC disruption.

The paper is organized as follows. Section 2 describes the sample and membership determination. Section 3 presents the tail-detection methods. Section 4 derives cluster properties. Section 5 gives the morphological analysis, orbital integration, and mass-segregation diagnostics. Section 6 presents the results, and Sect. 7 the discussion and conclusions.

## 2. Data

### 2.1. Initial sample

Our sample contains 65 OCs drawn from the catalog of Hunt & Reffert (2023, HR23), selected with $d < 500$ pc and age $\tau > 50$ Myr. The distance cut maximizes the precision of *Gaia* DR3 parallaxes after zero-point correction and limits systematic distance errors (Xu et al. 2025). The age cut excludes very young clusters still affected by gas-expulsion-driven violent relaxation, so any detected tidal structure should mainly trace gradual dynamical evolution. The HR23 catalog itself is affected by selection biases. Because it is built with density-based `HDBSCAN`, it preferentially recovers centrally concentrated overdensities and misses sparse, dynamically evolved, or partly dissolved systems; its membership is also magnitude-limited and increasingly incomplete toward faint, low-mass stars and crowded fields near the plane (Hunt & Reffert 2023, 2024). Our initial census is therefore conservative: diffuse tail members near the detection threshold may be missed, so the reported tail extents and member counts are best regarded as lower limits. We partly mitigate this by re-deriving membership with FFC (Sect. 3), which recovers fainter members than HR23.

### 2.2. Sample retrieval

To build a robust member census, we applied the FFC algorithm to *Gaia* DR3 sources within a 30° search radius, using the quality cuts and parallax zero-point corrections of Wei et al. (2025). The FFC algorithm systematically recovers more members than HR23 (Fig. 1a), improving sensitivity to faint tidal structures down to $G \sim 21$ mag. We tested the purity of extended tail candidates ($r > R_J$; 67–1121 tail stars per cluster) with equal-area control fields offset in Galactic longitude. The false-positive rates are low, typically $\lesssim$7% (for example, ~0.0% for Melotte 25), except for Melotte 111 (12.9%) because of a dense local background. These tests show that the extended features are overwhelmingly genuine tidal debris rather than field-star artifacts.

## 3. Methods

To identify tidal structures while limiting field contamination, we used a two-stage pipeline. The FFC algorithm first isolated core members and possible tail stars from the background. We then sequentially validated these candidates: 3D principal component analysis (PCA) removed projection artifacts through the alignment angle $\phi$, and physical checks plus the $L_z$–$E$ test verified consistency with the parent cluster.

### 3.1. 3D PCA analysis

Over secular timescales, OCs lose mass through relaxation and the Galactic tidal field, forming leading and trailing tails that trace their dynamical history (Baumgardt & Makino 2003; Just et al. 2009; Küpper et al. 2010). Because projected 2D morphologies are distorted along the line of sight, we use the 3D PCA framework of Xu et al. (2025) to recover the intrinsic geometry with minimal projection bias.

We applied PCA to the Galactocentric Cartesian coordinates $(X, Y, Z)$ of member stars to derive the main axis of spatial variance. Its orientation relative to the line of sight is measured by $\phi$: small $\phi$ values indicate elongation nearly along the line of sight and thus greater sensitivity to parallax errors, whereas large $\phi$ values imply a more reliable transverse structure. Following Xu et al. (2025), we adopted $\phi > 30^\circ$ to select robust tail candidates. Moderate changes to this threshold (25° or 35°) do not materially alter the confirmed sample because the later $L_z$–$E$ test provides an independent check. Clusters with $\phi < 30^\circ$ may still host real tails; Blanco 1 ($\phi = 4.06^\circ$), for example, has well-established tails (Meingast et al. 2021; Zhang et al. 2020; Risbud et al. 2025) and is retained as a supplementary reference case. Figure 1b shows the method for the high-$\phi$ cluster Mamajek 2. This step yielded 11 candidate OCs with possible tidal structures, comprising 4482 member stars.

### 3.2. $L_z$–$E$ test

To test the PCA candidates dynamically, we applied the 2D $L_z$–$E$ phase-space diagnostic ($L_z$: vertical angular momentum; $E$: orbital energy), following previous OC studies (Zhang et al. 2020; Risbud et al. 2025). In an axisymmetric Galactic potential, stars escaping from the same progenitor should remain clustered along a narrow locus in the $L_z$–$E$ plane because orbital energy and angular momentum are approximately conserved. We computed these quantities with the Milky Way potential of McMillan (2017). Due to the *Gaia* RVS limit ($G_{\rm RVS} \lesssim 14$), this check uses the bright subset with radial velocities; the fainter members are therefore validated mainly by morphology. For orbit integration, we adopted the cluster systemic RV, computed as the weighted mean of member RVs. A tight overlap between core stars and tail candidates then provides strong evidence of common origin (Risbud et al. 2025), as illustrated in Fig. B.1. Combined with distance checks, this test reduces the 11 PCA candidates to nine confirmed tidal-tail systems.

## 4. Cluster properties

### 4.1. Fundamental parameters

To derive the fundamental parameters of the nine confirmed tidal-tail clusters, including age, metallicity, color excess, distance modulus, and rotation, we fitted isochrones to the color–magnitude diagram (CMD), assuming that cluster members are coeval and chemically homogeneous. We use the latest PARSEC V2.0 models (Nguyen et al. 2025), whose updated physics and improved *Gaia* passbands, especially along the lower main sequence, reduce systematic biases in distance and age. The CMDs and best-fitting isochrones for all nine clusters are shown in Fig. A.1.

To test spatially varying extinction, we applied a star-by-star differential reddening correction to all nine confirmed tidal-tail clusters. For each cluster, we used the best-fitting PARSEC isochrone as the fiducial single-star sequence, measured the color residual $\Delta E(BP-RP)$ of each high-confidence member ($10 < G < 17$, RUWE $< 1.4$), removed the field-wide median as a global zero-point term, and interpolated the residual reddening with a distance-weighted $k$-nearest-neighbour estimator ($k = 15$), following Milone et al. (2012) as adapted to *Gaia* photometry. We then dereddened both color and magnitude using $A_G = 2.0\,E(BP-RP)$ and re-derived the binary fractions. The global offsets are small for all nine clusters ($|\Delta E(BP-RP)| \leq 0.024$ mag), showing that the mean reddening adopted in the isochrone fits is unbiased and leaves the fundamental parameters unchanged. The differential term $\sigma[\Delta E(BP{-}RP)]$ is likewise modest, below 0.065 mag for six clusters. Three nearby and extended systems (Mamajek 2, Theia 711, and Melotte 25) formally yield larger values ($\sigma \approx 0.11$–0.18 mag), but we treat these as upper limits: Melotte 25, at $\approx 47$ pc, is essentially unreddened, so its large formal $\sigma$ mainly reflects metallicity and line-of-sight depth effects absorbed by the single-isochrone reference. Rederiving the binary fractions on the corrected photometry does not change our conclusions (Sect. 7).

To estimate total mass and binary fraction, we adopted the method of Almeida et al. (2023), using age, metallicity, color excess, and distance modulus as priors. Monte Carlo simulations generate synthetic clusters that are matched to the observations to constrain the binary population and companion masses. A stellar mass function is then used to include unseen low-mass stars, stellar remnants, and unresolved binaries, yielding total cluster masses. The resulting parameters are listed in Table 1. Our derived ages, distances, and metallicities agree with previous *Gaia* DR3 determinations, where available (Hunt & Reffert 2023, 2024). For the best-studied cases, the Hyades (Melotte 25; log(age) = 9.05, $d \approx 47$ pc) and Coma Berenices (Melotte 111; log(age) = 8.70, $d \approx 86$ pc), our results match the literature within the quoted uncertainties. For the five clusters with newly reported tails (HSC 2765, Mamajek 2, Platais 12, Theia 711, UBC 11), Tables 1–2 provide, to our knowledge, the first dedicated structural and dynamical characterization.

### 4.2. Structure parameters

Star-cluster structure is often described with a King profile (King 1962), but this model assumes spherical symmetry and is poorly suited to systems with strong tidal distortions. We therefore adopt the two-component model of Zhong et al. (2022), which combines a King-law core with a log-Gaussian halo to describe both the inner cluster and the extended outer component. Using the characteristic radii $r_c$, $r_t$, $r_o$, and $r_e$, this model provides a more complete description of the density profile and evolutionary state

$$F(r) = f(r) + g(r), \tag{1}$$

$$f(r) = k \cdot \left( \frac{1}{\sqrt{1 + (r/r_c)^2}} - \frac{1}{\sqrt{1 + (r_t/r_c)^2}} \right)^2, \tag{2}$$

$$g(r) = \rho \cdot \exp\!\left( -\frac{(\ln r - \mu)^2}{2\sigma^2} \right), \tag{3}$$

where $k$ is a normalization constant, $r_c$ the core radius, and $r_t$ the tidal radius. The parameters $\rho$, $\mu$, and $\sigma$ describe the halo peak density, mean logarithmic radius, and dispersion. Figure 2 shows a representative fit.

### 4.3. Dynamical state and tidal parameters

To assess dynamical evolution, we compute the half-mass relaxation time, $t_{rh}$, the characteristic timescale for a self-gravitating system to approach dynamical equilibrium. Following

**Table 1.** Fundamental parameters of the nine OCs.

| Name | Mass ($M_\odot$) | $f_b$ | $r_c$ (pc) | $\phi$ (deg) | log(age) (year) | $m-M$ (mag) | $A_G$ (mag) | $Z$ | $\omega$ | $R_h$ |
|---|---|---|---|---|---|---|---|---|---|---|
| HSC_2765 | 100 ± 20 | 0.26 | 1.758 ± 0.879 | 73.785 | 8.10 | 7.14 | 0.28 | 0.020 | 0.300 | 3.282 ± 1.161 |
| Mamajek_2 | 316 ± 63 | 0.30 | 1.675 ± 0.838 | 39.128 | 8.05 | 7.22 | 0.68 | 0.020 | 0.300 | 3.128 ± 1.106 |
| Mamajek_4 | 864 ± 172 | 0.22 | 1.905 ± 0.952 | 75.417 | 8.80 | 8.39 | 0.14 | 0.020 | 0.800 | 2.893 ± 1.023 |
| Melotte 111 | 236 ± 47 | 0.24 | 3.796 ± 1.898 | 79.372 | 8.80 | 4.98 | 0.10 | 0.020 | 0.300 | 7.087 ± 2.507 |
| Melotte_22 | 1276 ± 255 | 0.21 | 1.047 ± 0.523 | 81.872 | 7.90 | 6.29 | 0.32 | 0.020 | 0.600 | 1.954 ± 0.691 |
| Melotte_25 | 597 ± 119 | 0.33 | 8.793 ± 4.397 | 67.446 | 8.65 | 4.03 | 0.42 | 0.020 | 0.300 | 16.416 ± 5.806 |
| Platais_12 | 384 ± 76 | 0.23 | 0.699 ± 0.349 | 51.109 | 8.00 | 8.69 | 0.34 | 0.020 | 0.300 | 1.304 ± 0.461 |
| Theia_711 | 226 ± 45 | 0.22 | 1.289 ± 0.645 | 37.361 | 8.10 | 8.78 | 0.74 | 0.020 | 0.300 | 2.406 ± 0.851 |
| UBC_11 | 190 ± 38 | 0.23 | 1.004 ± 0.502 | 84.877 | 7.80 | 8.85 | 0.36 | 0.020 | 0.300 | 1.874 ± 0.663 |

**Notes.** Columns list cluster name, mass, binary fraction ($f_b$), core radius ($r_c$), the angle $\phi$ between the first PCA axis and the line of sight, half-mass radius ($R_h$), and the fundamental parameters (log(age), $m - M$, $A_V$, $Z$, $\omega$) from PARSEC v2.0 isochrone fitting.

**Table 1.** continued.

| Name | $r_t$ (pc) | $r_e$ (pc) | $r_{50}$ (pc) | $R_J$ (pc) | $t_{rh}$ (Myr) | $\rho_{amb}$ ($M_\odot$/pc$^3$) | $M_{ini}$ ($M_\odot$) | $t_{95}$ (Gyr) |
|---|---|---|---|---|---|---|---|---|
| HSC_2765 | 21.978 ± 10.989 | 7.044 ± 0.418 | 2.429 | 3.527 ± 0.060 | 29.793 ± 16.297 | 0.138 | 279.627 | 0.264 |
| Mamajek_2 | 20.943 ± 10.471 | 14.759 ± 2.017 | 2.919 | 5.156 ± 0.078 | 36.368 ± 19.541 | 0.131 | 562.286 | 0.398 |
| Mamajek_4 | 23.808 ± 11.904 | 8.299 ± 1.599 | 2.572 | 7.384 ± 0.170 | 44.895 ± 24.108 | 0.122 | 3742.347 | 1.208 |
| Melotte 111 | 47.455 ± 23.728 | 31.285 ± 9.877 | 6.108 | 5.026 ± 0.078 | 151.107 ± 81.112 | 0.115 | 1334.971 | 0.729 |
| Melotte_22 | 13.086 ± 6.543 | 4.814 ± 0.322 | 1.727 | 8.781 ± 0.133 | 35.480 ± 18.935 | 0.125 | 1980.051 | 0.864 |
| Melotte_25 | 109.924 ± 54.962 | 339.054 ± 271.243 | 18.257 | 6.595 ± 0.015 | 1095.423 ± 582.143 | 0.130 | 4798.192 | 1.438 |
| Platais_12 | 8.735 ± 4.367 | 26.160 ± 20.928 | 1.170 | 5.351 ± 0.119 | 9.683 ± 5.226 | 0.141 | 975.754 | 0.549 |
| Theia_711 | 16.113 ± 8.057 | 4.197 ± 0.583 | 1.929 | 4.660 ± 0.067 | 20.160 ± 10.876 | 0.144 | 485.510 | 0.350 |
| UBC_11 | 12.552 ± 6.276 | 7.029 ± 0.743 | 1.703 | 4.109 ± 0.095 | 11.147 ± 6.114 | 0.140 | 473.769 | 0.346 |

**Notes.** Columns list cluster name, tidal radius ($r_t$), effective radius ($r_e$), half-mass radius ($r_{50}$), Jacobi radius ($R_J$), half-mass relaxation time ($t_{rh}$), ambient stellar density ($\rho_{amb}$), initial mass ($M_{ini}$), and dynamical lifetime ($t_{95}$).

**Table 2.** Orbital parameters of the nine OCs.

| Name | $T_r$ (Myr) | $R_{peri}$ (kpc) | $R_{apo}$ (kpc) | $e$ | $z_{max}$ (pc) | $X$ (kpc) | $Y$ (kpc) | $Z$ (kpc) | $U$ (km/s) | $V$ (km/s) | $W$ (km/s) |
|---|---|---|---|---|---|---|---|---|---|---|---|
| HSC_2765 | 157.232 | 7.280 | 7.864 | 0.039 | 41.064 | 7.790 | –0.106 | 0.020 | 13.792 | 215.533 | –2.779 |
| Mamajek_2 | 149.689 | 6.790 | 7.814 | 0.070 | 67.534 | 7.814 | 0.059 | 0.063 | –0.303 | 206.471 | 2.270 |
| Mamajek_4 | 146.074 | 6.272 | 8.019 | 0.122 | 162.930 | 7.591 | –0.126 | –0.109 | 33.229 | 205.927 | –8.929 |
| Melotte 111 | 174.020 | 7.920 | 8.683 | 0.046 | 133.113 | 8.009 | –0.004 | 0.107 | –8.861 | 226.659 | 4.781 |
| Melotte_22 | 155.403 | 7.006 | 8.126 | 0.074 | 102.745 | 8.120 | 0.029 | –0.033 | –3.692 | 204.236 | –7.114 |
| Melotte_25 | 164.330 | 7.393 | 8.411 | 0.064 | 163.943 | 8.044 | 0.000 | 0.004 | 17.967 | 215.463 | 11.433 |
| Platais_12 | 169.179 | 7.724 | 8.486 | 0.047 | 10.900 | 7.720 | –0.341 | 0.009 | 12.217 | 229.716 | 0.399 |
| Theia_711 | 146.022 | 6.682 | 7.618 | 0.066 | 57.329 | 7.616 | 0.188 | –0.002 | –5.368 | 207.808 | –4.576 |
| UBC_11 | 172.212 | 7.607 | 8.848 | 0.075 | 42.137 | 7.626 | –0.240 | –0.037 | 13.692 | 235.174 | 0.703 |

Spitzer & Shull (1975), we use

$$t_{rh} = (8.9 \times 10^5\ \mathrm{yr})\, \frac{M_{\rm clu}^{1/2} R_h^{3/2}}{\langle m \rangle \log_{10}(0.4 M_{\rm clu}/\langle m \rangle)}, \tag{4}$$

where $M_{\rm clu}$ is the total cluster mass, $\langle m \rangle$ the mean stellar mass, and $R_h$ the half-mass radius. Because $R_h$ is not fitted directly, we estimate it from the structural parameters of Sect. 4.1 using the scaling relation of Angelo et al. (2025)

$$R_h = 0.547 \times r_c \times \left(\frac{r_t}{r_c}\right)^{0.486}. \tag{5}$$

To quantify survival against tidal disruption, we estimate the dissolution time $t_{95}$, the time required for a cluster to lose 95% of its initial mass. Using the semi-analytical model of Lamers et al. (2005), we solve

$$0.05 = \left[\mu_{\rm ev}(t_{95})^{\gamma} - \frac{\gamma t_{95}}{t_0} M_{\rm ini}^{-\gamma}\right]^{1/\gamma}, \tag{6}$$

$$M_{\rm ini} = \frac{\left[M_{\rm clu}^{\gamma} + \frac{\gamma t_{\rm age}}{t_0}\right]^{1/\gamma}}{\mu_{\rm ev}(t_{\rm age})}. \tag{7}$$

Here $\gamma = 0.62$ is a dimensionless index, $t_0 = 810$ Myr $(1-\epsilon)\ 10^{-4\gamma} \rho_{\rm amb}^{-1/2}$ is the disruption parameter, $\epsilon$ is the orbital

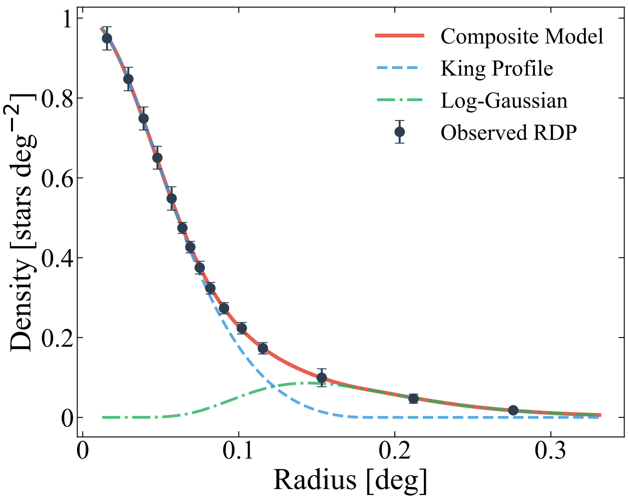


**Fig. 2.** Example structural fit. Radial density profile (RDP) of NGC 2972. Black points show the data; the red curve is the two-component model, combining a King profile (dashed blue) for the inner region and a log-Gaussian term (dash-dotted green) for the extended outer structure.

eccentricity, and $\mu_{\rm ev}(t)$ describes stellar-evolution mass loss (Lamers et al. 2005). The ambient density is derived from the Galactic potential through Poisson's equation, $\rho_{\rm amb} = \nabla^2\Phi_{\rm G}/(4\pi G)$.

To distinguish bound members from tidal debris, we compute the Jacobi radius $R_J$, which defines the theoretical limit of the cluster's gravitational influence. For a cluster in an axisymmetric Galactic potential (Angelo et al. 2025), we use

$$R_J = \left(\frac{GM_{\rm clu}}{\lambda_{e,1}}\right)^{1/3}, \tag{8}$$

where $\lambda_{e,1}$ is the effective tidal frequency, i.e., the maximum eigenvalue of the tidal tensor. The Galactic potential $\Phi_{\rm G}$ is written as the sum of bulge ($\Phi_B$), disk ($\Phi_D$), and halo ($\Phi_H$) terms, following Haghi et al. (2015) and Sanderson et al. (2017)

$$\lambda_{e,1} = -\frac{\partial^2\Phi_{\rm G}}{\partial x^2} - \frac{\partial^2\Phi_{\rm G}}{\partial z^2}, \tag{9}$$

$$\Phi_B = -\frac{GM_B}{r + r_B}, \tag{10}$$

$$\Phi_D = -\frac{GM_D}{\sqrt{x^2 + y^2 + \left(a + \sqrt{z^2 + b^2}\right)^2}}, \tag{11}$$

$$\Phi_H = -\frac{GM_S}{(\ln 2)/2 \cdot r}\frac{\ln(1 + r/r_s)}{r}. \tag{12}$$

Here $r$ is the Galactocentric distance. We adopt the standard parameter set: $M_B = 2.5 \times 10^{10}\,M_\odot$, $r_B = 0.5$ kpc, $M_D = 7.5 \times 10^{10}\,M_\odot$, $a = 5.4$ kpc, and $b = 0.3$ kpc (Haghi et al. 2015); for the halo, $M_S = 1.87 \times 10^{11}\,M_\odot$ and $r_s = 15.19$ kpc (Sanderson et al. 2017).

## 5. Tidal tail analysis

### 5.1. Morphology analysis

We analyzed tidal-tail morphology in the tangential plane, which projects the 3D stellar distribution onto a 2D plane centered on the cluster and provides a convenient view of extended structures. This projection complements the PCA-based identification of the main variance axis and allows direct measurement of tail orientation and extent. We computed the relative tangential coordinates ($\Delta\alpha$, $\Delta\delta$) of each star with Eqs. (13) and (14)

$$\Delta\alpha = \cos(\delta)\sin(\alpha - \alpha_0), \tag{13}$$

$$\Delta\delta = \sin(\delta)\cos(\delta_0) - \cos(\delta)\sin(\delta_0)\cos(\alpha - \alpha_0). \tag{14}$$

Here $\alpha$ and $\delta$ are the stellar right ascension and declination, and $\alpha_0$ and $\delta_0$ are the cluster means. Figure 3 shows the tangential projections of the nine OCs and their extended tidal morphologies.

We used the Jacobi radius $R_J$ (Eq. (8)) to define the stripping boundary and separate core members from debris. For visualization and classification, $R_J$ is converted from physical units to an angular radius using the heliocentric distance of each cluster.

To quantify tail extent, we adopted a model-independent approach. We first located the 3D cluster centroid and selected the 10% most distant stars as tracers. A singular value decomposition (SVD) of these tracers gives the main linear tail axis, onto which all members are projected. The resulting projected chord length is the separation between the two most distant projected points. Because real tails are curved, this metric provides a robust lower limit to their true extent.

### 5.2. Orbit

We integrated each cluster orbit forward and backward for five orbital periods with the `galpy` `MWPotential2014` model, which includes a Miyamoto-Nagai disk, a spherical power-law bulge, and an NFW halo. We adopted $R_0 = 8$ kpc, $V_0 = 220$ km/s, and $z = 20.8$ pc, and used each cluster's proper motion, heliocentric distance, equatorial coordinates, and mean *Gaia* DR3 radial velocity as input. Representative 3D trajectories are shown in Fig. B.1, and the orbital parameters are listed in Table 2.

Using these simulated orbits, we refined the tail-length estimate to account for stream curvature. By projecting member stars directly onto the orbital path rather than onto a linear axis, we measured the orbital arc length of each tail. This metric corrects the curvature bias of the SVD-based chord length and therefore better captures the true extent of the disruption. As shown in Fig. 4, the two measures agree well for most clusters (for example, Mamajek 2, Mamajek 4, and Melotte 25), indicating that the tails are highly collimated and closely follow their orbits. UBC 11 is the main exception: its SVD length exceeds the orbital arc length, implying a more complex morphology or off-orbit debris.

### 5.3. Mass segregation

Mass segregation is a key signature of cluster dynamical evolution. We quantified it with the mass segregation ratio ($\Lambda_{\rm MSR}$) of Allison et al. (2009), widely used to detect stratification in stellar systems (Bhattacharya et al. 2022; Tarricq et al. 2022; Zhang et al. 2020; Angelo et al. 2025).

The calculation is based on the minimum spanning tree (MST). We measured the MST length ($l_{\rm massive}$) of the most massive stars $N_{\rm massive}$ and compared it with the mean MST length ($\langle l_{\rm random}\rangle$) of $N$ random subsets of the same size drawn from the full cluster sample. The ratio is

$$\Lambda_{\rm MSR}(N) = \frac{\langle l_{\rm random}\rangle}{l_{\rm massive}} \pm \frac{\sigma_{\rm random}}{l_{\rm massive}}, \tag{15}$$

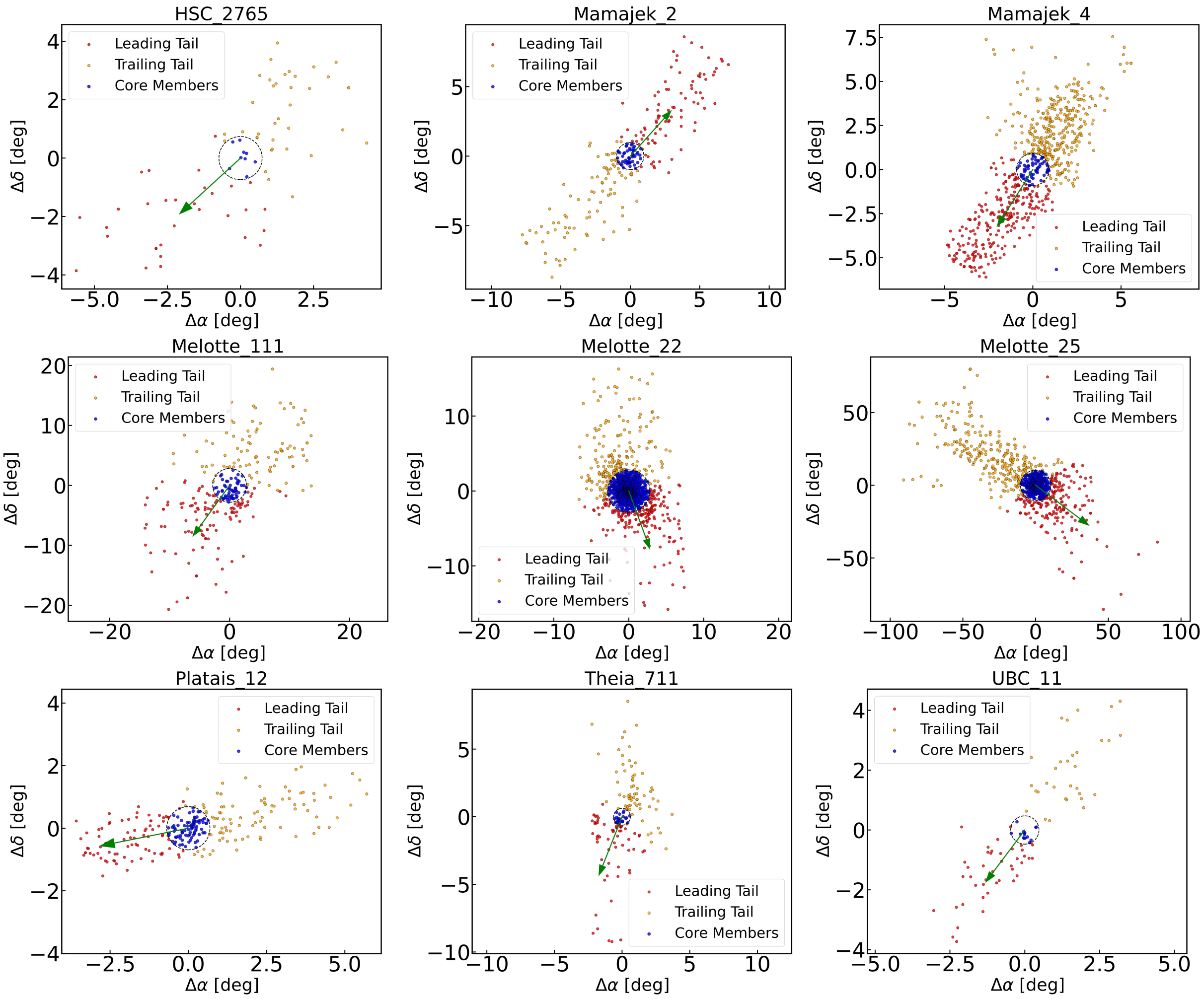


**Fig. 3.** Spatial distributions of the core members (blue dots) of the nine OCs, with the detected tide tails indicated by red and yellow dots. The dotted black circle indicates the Jacobi radius, and the green arrow indicates the expected direction of movement along the star cluster's orbit. The layout of this figure follows the presentation style introduced by Sharma et al. (2025).

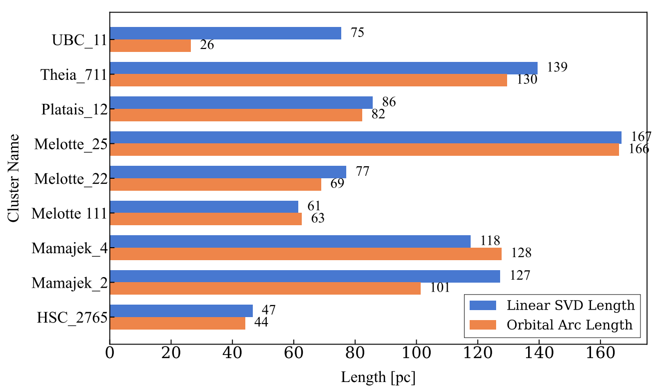


**Fig. 4.** Comparison of tidal tail lengths measured by linear SVD projection (dark blue) and orbital arc length (teal). The orbital arc length accounts for the curvature of the tails and generally provides a more accurate (and often longer) estimate of the true physical extent.

where $\sigma_{\rm random}$ is the standard deviation of the random-trial MST lengths. We used $N = 100$ iterations and restricted all samples to members brighter than $G < 18.5$ to reduce incompleteness bias.

The index depends on $N_{\rm massive}$: values significantly above unity indicate mass segregation, and persistent elevation at larger $N_{\rm massive}$ implies that segregation extends to a broader mass range. We therefore computed $\Lambda_{\rm MSR}$ from $N_{\rm massive} = 5$ upward, capping the calculation at $N_{\rm massive} = 100$ for clusters with more than 100 members.

Across the full sample, mass segregation is ubiquitous. As shown in Fig. B.1 (left panels), all nine clusters have $\Lambda_{\rm MSR} > 1$ for their most massive members ($N_{\rm massive} \lesssim 20$), confirming that massive stars are more centrally concentrated. Mamajek 2 provides a clear example: $\Lambda_{\rm MSR}$ is high for the most massive stars and declines toward unity as lower-mass stars are included. The strongest signals ($\Lambda_{\rm MSR} > 2$) occur in Mamajek 4, Melotte 25, Melotte 111, Platais 12, and Theia 711, indicating more advanced dynamical evolution.

We also examined whether segregation strength correlates with bulk cluster properties. It does not follow chronological age in a simple monotonic way: the strongly segregated systems span log(age) ≈ 8.0–9.1 and include both old (Melotte 25, Mamajek 4) and relatively young (Theia 711, Platais 12) clusters. A clearer trend appears with dynamical age, i.e., the number of elapsed half-mass relaxation times ($\tau/t_{rh}$); the largest $\Lambda_{\rm MSR}$ values generally occur in clusters that have evolved through many relaxation times, consistent with two-body relaxation as the main driver. More compact denser clusters (smaller $R_h$, shorter $t_{rh}$) also tend to be more strongly segregated. However, with only nine systems and sizable uncertainties, these trends remain suggestive rather than definitive.

## 6. Results

We carried out a systematic *Gaia* DR3 search for tidal structures in 65 nearby OCs ($d < 500$ pc). Combining 3D PCA with orbital analysis, we identified tidal tails in nine clusters, including five new detections (HSC 2765, Mamajek 2, Platais 12, Theia 711, and UBC 11), and we refined the structural parameters of four previously known systems. We also introduce the orbital arc length as a physically motivated measure of tail extent, obtaining lengths of 26–166 pc. These clusters are dynamically evolved, as indicated by widespread mass segregation and half-mass relaxation times shorter than their ages.

The nine detections are best interpreted in the context of the full 65-cluster sample. The 3D PCA preselection flagged 11 clusters with significant elongation ($\phi > 30°$); the subsequent $L_z$–$E$ and distance checks rejected two. One showed no coherent outer locus in the $L_z$–$E$ plane despite its large member sample, indicating contamination rather than genuine debris. The other lay too close to the $\phi = 30°$ threshold to separate intrinsic elongation from line-of-sight broadening. The remaining ~54 clusters generally show weaker projected elongation and, on average, shorter relaxation times relative to their ages or more compact morphologies, so any stripped debris likely remains near the Jacobi radius and below our overdensity threshold. This does not imply an absence of tails; within our conservative, contamination-limited pipeline (Sect. 2), they are simply too faint, too foreshortened, or too contaminated to satisfy both the morphological and dynamical criteria. The nine confirmed systems are thus the subset with debris that is bright enough, favorably oriented, and dynamically coherent.

Among the newly detected systems, Mamajek 2 and Theia 711 show the most prominent tails, with orbital arc lengths of ~101 pc and ~130 pc. Platais 12 also has an extended structure of ~82 pc. HSC 2765 and UBC 11 are more compact, at ~44 pc and ~26 pc. The short tail in UBC 11 illustrates the sensitivity of the 3D PCA method to subtle dynamical signatures.

For previously known tidal systems, our orbit-based lengths add new constraints. In Mamajek 4, we measure a tail length of ~128 pc and identify 655 members, much smaller than the ~725 pc extent reported by Kos (2024), likely because our estimate is restricted to the kinematically and morphologically coherent structure. For Melotte 111, our arc length of ~63 pc agrees well with Risbud et al. (2025). For the Hyades clusters (Melotte 22 and Melotte 25), our arc lengths of ~69 pc and ~166 pc are more conservative than some extreme literature values (e.g., the ~800 pc extent obtained when Hyades members are linked to $N$-body predictions; Jerabkova et al. 2021), supporting a more compact debris distribution for the kinematically and morphologically confirmed members recovered here. Melotte 25 also stands out dynamically, with the largest half-mass relaxation time ($t_{rh} \approx 1095$ Myr, with ~53% relative uncertainty) and the largest half-mass radius in the sample ($r_{50} = 18.3$ pc). Its binary fraction, measured with differential-reddening-corrected photometry, is $f_b \approx 0.33$ overall and $\approx 0.41$ in the core, fully consistent with the Hyades multiplicity frequency of ~40% from long-term spectroscopic monitoring (Torres et al. 2026). These properties likely reflect its advanced dynamical evolution and extensive tidal disruption, which has redistributed much of its original low-mass and wide-binary population into the field.

The most important dynamical result is the ubiquity of mass segregation. As shown in Sect. 5.3, all nine clusters have $\Lambda_{\rm MSR} > 1$ for their most massive members, with especially strong signals ($\Lambda_{\rm MSR} > 2$) in Mamajek 4, Melotte 25, Melotte 111, Platais 12, and Theia 711. These systems have therefore experienced sufficient two-body relaxation to move massive stars inward and low-mass stars outward. Their half-mass relaxation times are also much shorter than their ages (Table 1), independently confirming that they are dynamically relaxed.

The co-occurrence of mass segregation and tidal tails in all nine clusters points to a single physical pathway. Two-body relaxation drives loosely bound low-mass stars to the cluster outskirts, where the Galactic tidal field can strip them most efficiently (Baumgardt & Makino 2003). The resulting debris should therefore be biased toward low masses, as expected for evaporation-dominated tails (Küpper et al. 2010). Internal relaxation coupled with external stripping thus governs the long-term mass loss and eventual dissolution of evolved OCs in the solar neighborhood (Lamers et al. 2005).

## 7. Discussion and conclusions

*Gaia* astrometry now allows the detailed morphology of tidal tails to be linked directly to the internal dynamics that produces them. We focus here on how mass stratification drives cluster dissolution and how binary populations complicate that classical picture.

### 7.1. Mass stratification driving cluster dissolution

Our results show a direct link between internal two-body relaxation and external tidal stripping. All nine tail-bearing clusters display clear mass segregation, which moves loosely bound low-mass stars to the outskirts, where the Galactic tidal field removes them efficiently. The resulting debris is therefore biased toward low masses (Küpper et al. 2010). Its ubiquity in our sample indicates that mass stratification is a primary driver of long-term mass loss and eventual OC dissolution (Baumgardt & Makino 2003; Lamers et al. 2005).

### 7.2. Binary populations testing the stratification model

The classical stratification picture predicts that single low-mass stars are preferentially ejected while massive binaries sink toward the core (Baumgardt & Makino 2003). Recent work challenges this view by finding substantial binary fractions in tidal tails (Pang et al. 2023; Sharma et al. 2025). Notably, Sharma et al. (2025) found tail binary fractions comparable to or higher than those in the parent cores, and high multiplicity is well established even in dynamically old systems such as the Hyades (Torres et al. 2026). Our photometric analysis offers a direct test. Using differential-reddening-corrected photometry, we find comparable high-mass-ratio binary fractions in the core and tail of Mamajek 4 ($f_{b,\rm core} = 0.20 \pm 0.05$ and $f_{b,\rm tail} = 0.22 \pm 0.02$). Across the full sample the core and tail fractions are statistically consistent in most clusters; the core exceeds the tail at $>1.5\sigma$ only in Mamajek 2 and Melotte 25, which also have the largest differential reddening ($\sigma[\Delta E(BP-RP)] \gtrsim 0.11$ mag). This excess is therefore more plausibly due to residual reddening enhancing the binary sequence in denser cores than to a true dynamical difference. Even allowing for observational uncertainty, the sizable binary population in the debris implies that simple mass stratification alone cannot explain the ejection process. Dynamical heating and close encounters likely help transport massive binaries into the tails. A larger homogeneous sample will be needed to quantify their relative roles.

### 7.3. Conclusions

Using *Gaia* DR3 astrometry, we investigated the interplay between tidal tails and mass segregation in 65 nearby open clusters. By combining density-based clustering with morphological and dynamical diagnostics, we built a robust pipeline for tidal-debris detection and coupled it with MST analysis to test how internal relaxation and external stripping act together.

We summarize our primary findings below:

1. We detect tidal tails in nine clusters, including five new cases: HSC 2765, Mamajek 2, Platais 12, Theia 711, and UBC 11. These detections are supported by rigorous membership identification and phase-space validation;
2. Mass segregation is present in all nine tail-bearing clusters. Massive stars are centrally concentrated, whereas low-mass stars preferentially occupy the outskirts. The strongest signals occur in Mamajek 4, Melotte 25, Melotte 111, Platais 12, and Theia 711;
3. All nine systems are dynamically relaxed: their half-mass relaxation times are much shorter than their ages. They move on low-eccentricity thin-disk orbits, and their tails broadly follow those orbital paths;
4. The co-occurrence of mass segregation and tidal tails directly supports a coupled evolutionary mechanism: two-body relaxation moves loosely bound low-mass stars to the outskirts, and the Galactic tidal field then strips them to form tidal debris. This interplay drives the eventual dissolution of evolved open clusters.

Wenchang Zhao (W.Z.) analyzed the data, developed the pipeline, and drafted the manuscript. Jing Chen (J.C.) conceived and supervised the project and revised the manuscript. Yujun Tang (Y.T.), Xuran He (X.H.), Zhengke Deng (Z.D.), Lishuai Huang (L.H.), and Lin Fu (L.F.) contributed to data processing and revision. Huanbin Chi (H.C.) and Su Zhang (S.Z.) contributed to data processing, discussion, and revision.

## Data availability

The data underlying this article are available on Zenodo at https://doi.org/10.5281/zenodo.20666952.

*Acknowledgements.* This work was supported by the National Natural Science Foundation of China (NSFC; No. 12363004) and the Special Basic Cooperative Research Programs of the Yunnan Provincial Undergraduate Universities' Association (Nos. 202101BA070001-215 and 202301BA070001-049). This work used data from the European Space Agency *Gaia* mission, available at https://www.cosmos.esa.int/gaia. Data processing and analysis were carried out by the *Gaia* Data Processing and Analysis Consortium (DPAC; https://www.cosmos.esa.int/web/gaia/dpac/consortium), supported by national institutions, especially those participating in the *Gaia* Multilateral Agreement.

## References

Allison, R. J., Goodwin, S. P., Parker, R. J., et al. 2009, MNRAS, 395, 1449
Almeida, A., Monteiro, H., & Dias, W. S. 2023, MNRAS, 525, 2315
Angelo, M. S., Santos, J. F. C., Corradi, W. J. B., & Maia, F. F. S. 2025, MNRAS, 539, 2513
Baumgardt, H., & Makino, J. 2003, MNRAS, 340, 227
Bhattacharya, S., Rao, K. K., Agarwal, M., Balan, S., & Vaidya, K. 2022, MNRAS, 517, 3525
Chen, Z., Goldwasser, J., Tuckman, P., et al. 2022, Nat. Commun., 13, 3538
Childs, A. C., Geller, A. M., von Hippel, T., Motherway, E., & Zwicker, C. 2024, ApJ, 962, 41
Haghi, H., Zonoozi, A. H., & Taghavi, S. 2015, MNRAS, 450, 2812
Hunt, E. L., & Reffert, S. 2023, A&A, 673, A114
Hunt, E. L., & Reffert, S. 2024, A&A, 686, A42
Jadhav, V. V., Risbud, D., Kroupa, P., & Wu, W. 2025, A&A, 704, A50
Jerabkova, T., Boffin, H. M. J., Beccari, G., et al. 2021, A&A, 647, A137
Just, A., Berczik, P., Petrov, M. I., & Ernst, A. 2009, MNRAS, 392, 969
King, I. 1962, ApJ, 67, 471
Kos, J. 2024, A&A, 691, A28
Kroupa, P., Pflamm-Altenburg, J., Mazurenko, S., et al. 2024, ApJ, 970, 94
Küpper, A. H. W., Kroupa, P., Baumgardt, H., & Heggie, D. C. 2010, MNRAS, 401, 105
Lamers, H. J. G. L. M., Gieles, M., & Portegies Zwart, S. F. 2005, A&A, 429, 173
McMillan, P. J. 2017, MNRAS, 465, 76
Meingast, S., & Alves, J. 2019, A&A, 621, L3
Meingast, S., Alves, J., & Rottensteiner, A. 2021, A&A, 645, A84
Milone, A. P., Piotto, G., Bedin, L. R., et al. 2012, A&A, 540, A16
Motherway, E., Geller, A. M., Childs, A. C., Zwicker, C., & von Hippel, T. 2024, ApJ, 962, L9
Nguyen, C. T., Costa, G., Bressan, A., et al. 2025, A&A, 701, A258
Pang, X., Wang, Y., Tang, S.-Y., et al. 2023, AJ, 166, 110
Risbud, D., Jadhav, V. V., & Kroupa, P. 2025, A&A, 694, A258
Röser, S., Schilbach, E., & Goldman, B. 2019, A&A, 621, L2
Sanderson, R. E., Hartke, J., & Helmi, A. 2017, ApJ, 836, 234
Sharma, I., Jadhav, V., Subramaniam, A., & Wirth, H. 2025, A&A, 704, A167
Spitzer, Jr., L., & Shull, J. M. 1975, ApJ, 201, 773
Tarricq, Y., Soubiran, C., Casamiquela, L., et al. 2022, A&A, 659, A59
Torres, G., Stefanik, R. P., & Latham, D. W. 2026, ApJS, 283, 81
Wei, X., Chen, J., Zhang, S., et al. 2025, AJ, 169, 115
Xu, M., Fu, X., Chen, Y., et al. 2025, A&A, 698, A156
Zhang, S. 2026, AJ, 171, 236
Zhang, Y., Tang, S.-Y., Chen, W. P., Pang, X., & Liu, J. Z. 2020, ApJ, 889, 99
Zhang, S., Chen, J., Wei, X., et al. 2025, Phys. Rev. D, 111, 123026
Zhong, J., Chen, L., Jiang, Y., Qin, S., & Hou, J. 2022, AJ, 164, 54
Zwicker, C., Geller, A. M., Childs, A. C., Motherway, E., & von Hippel, T. 2024, ApJ, 967, 44

## Appendix A: CMDs of the nine tidal-tail clusters

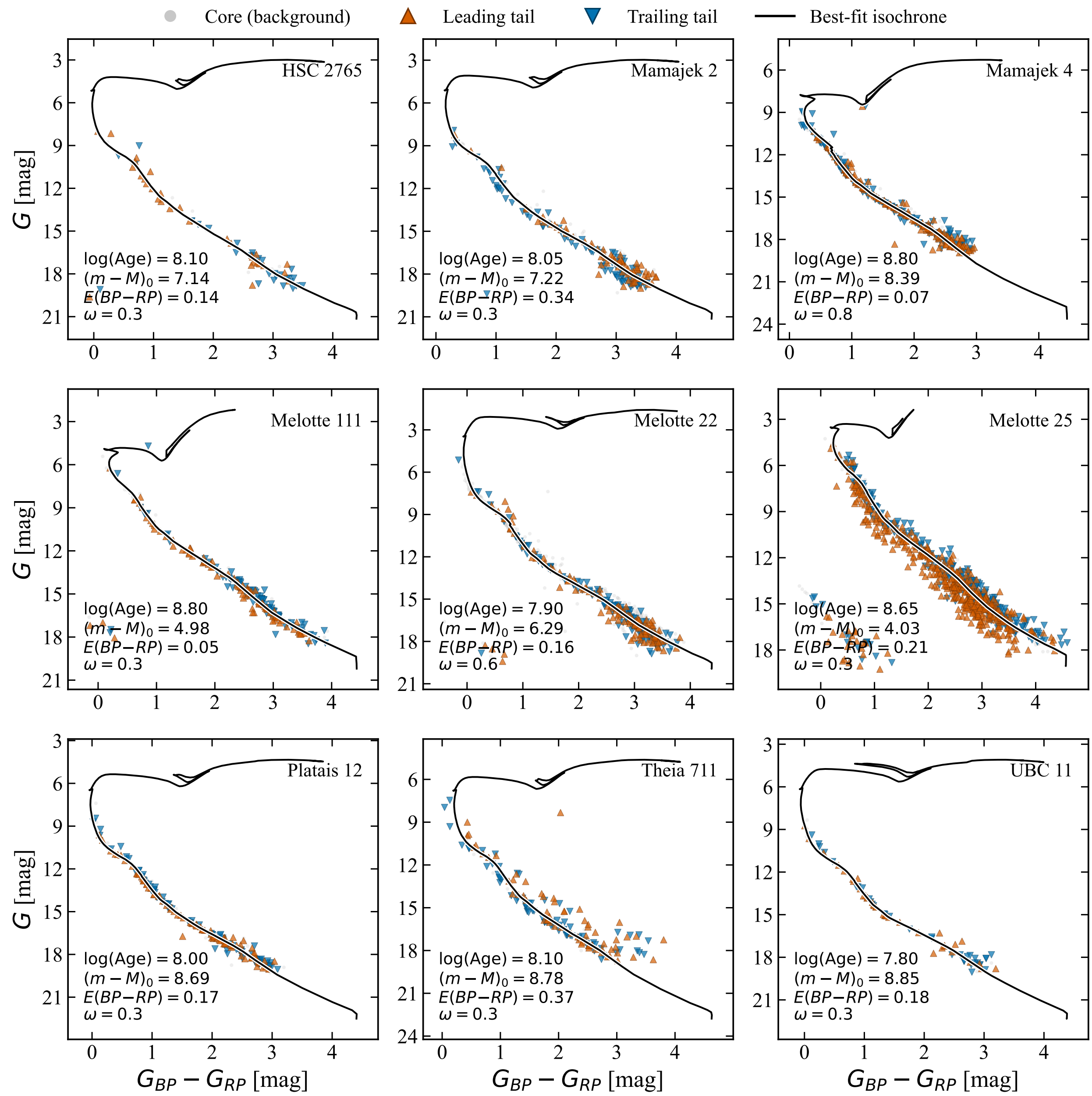


Fig. A.1: CMDs of the nine tidal-tail clusters, with the best-fitting PARSEC v2.0 isochrone (solid line) overlaid on the member photometry.

## Appendix B: Plots of newly discovered tidal tails

This appendix presents the five newly discovered tidal-tail candidates: HSC 2765, Mamajek 2, Platais 12, Theia 711, and UBC 11. For each cluster, the panels show (left to right) the mass-segregation analysis, the $L_z$–$E$ phase-space distribution, and the 3D orbital trajectory. In the scatter plots, blue marks core members, red the leading tail, and yellow the trailing tail.

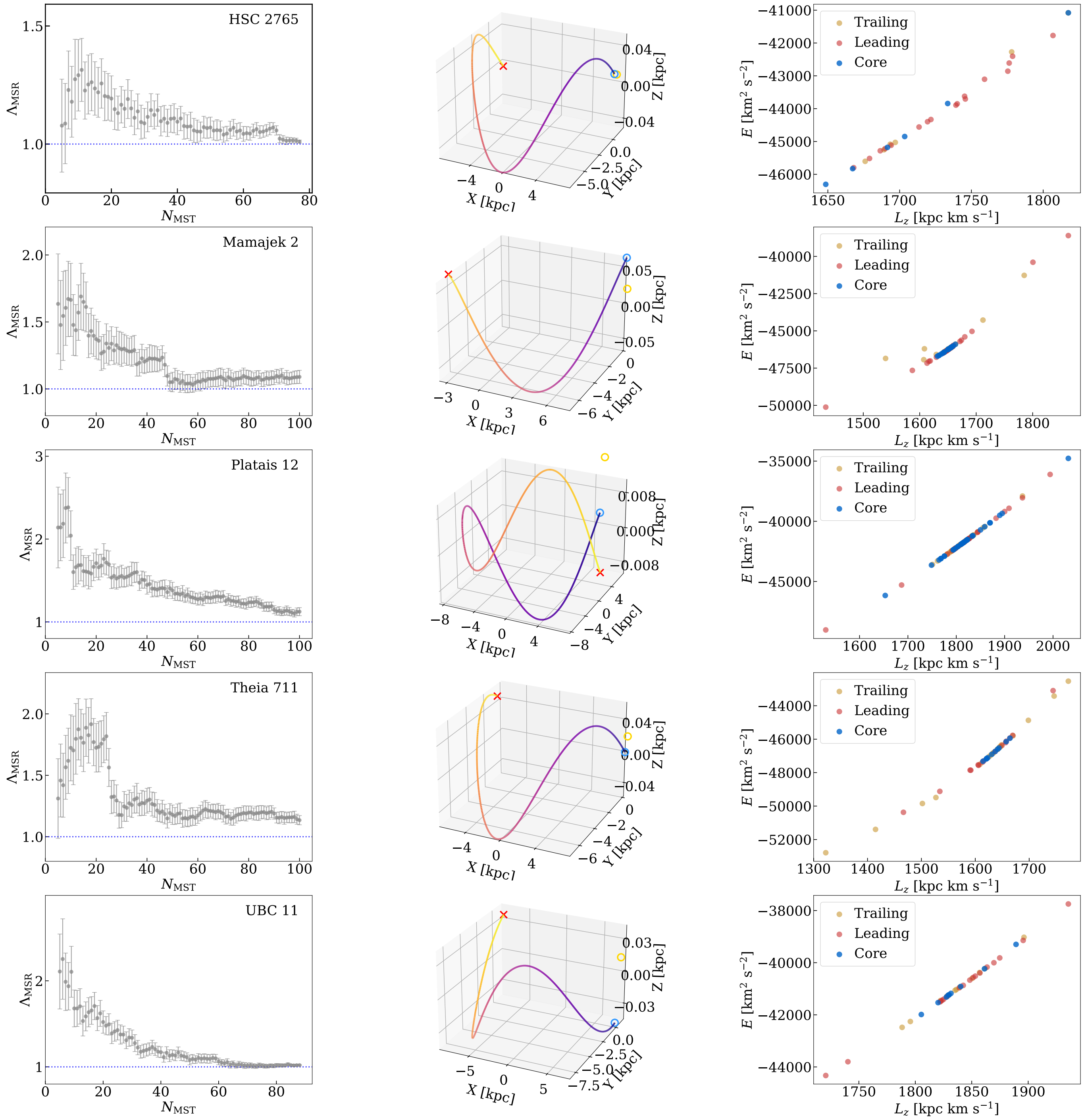


Fig. B.1: Detailed plots of the five newly discovered tidal-tail candidates. From top to bottom: HSC 2765, Mamajek 2, Platais 12, Theia 711, and UBC 11. For each cluster, the panels show (left to right) the mass-segregation analysis, the $L_z$–$E$ phase-space distribution, and the 3D orbital trajectory. Blue, red, and yellow mark core, leading-tail, and trailing-tail members. The first panel of each row lists the cluster name and key parameters.